



UvA-DARE (Digital Academic Repository)

Confirmation of Water Absorption in the Thermal Emission Spectrum of the Hot Jupiter WASP-77Ab with HST/WFC3

Mansfield, M.; Wisser, L.; Stevenson, K.B.; Smith, P.; Line, M.R.; Bean, J.L.; Fortney, J.J.; Parmentier, V.; Kempton, E.M.-R.; Arcangeli, J.; Desert, J.-M. ; Kilpatrick, B.; Kreidberg, L.; Malik, M.

DOI

[10.3847/1538-3881/ac658f](https://doi.org/10.3847/1538-3881/ac658f)

Publication date

2022

Document Version

Final published version

Published in

The Astronomical Journal

License

CC BY

[Link to publication](#)

Citation for published version (APA):

Mansfield, M., Wisser, L., Stevenson, K. B., Smith, P., Line, M. R., Bean, J. L., Fortney, J. J., Parmentier, V., Kempton, EM-R., Arcangeli, J., Desert, J-M., Kilpatrick, B., Kreidberg, L., & Malik, M. (2022). Confirmation of Water Absorption in the Thermal Emission Spectrum of the Hot Jupiter WASP-77Ab with HST/WFC3. *The Astronomical Journal*, 163(6), [261]. <https://doi.org/10.3847/1538-3881/ac658f>

General rights

It is not permitted to download or to forward/distribute the text or part of it without the consent of the author(s) and/or copyright holder(s), other than for strictly personal, individual use, unless the work is under an open content license (like Creative Commons).

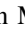

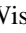








Disclaimer/Complaints regulations

If you believe that digital publication of certain material infringes any of your rights or (privacy) interests, please let the Library know, stating your reasons. In case of a legitimate complaint, the Library will make the material inaccessible and/or remove it from the website. Please Ask the Library: <https://uba.uva.nl/en/contact>, or a letter to: Library of the University of Amsterdam, Secretariat, Singel 425, 1012 WP Amsterdam, The Netherlands. You will be contacted as soon as possible.

UvA-DARE is a service provided by the library of the University of Amsterdam (<https://dare.uva.nl>)



Confirmation of Water Absorption in the Thermal Emission Spectrum of the Hot Jupiter WASP-77Ab with HST/WFC3

Megan Mansfield^{1,11} , Lindsey Wiser² , Kevin B. Stevenson³ , Peter Smith², Michael R. Line² , Jacob L. Bean⁴ , Jonathan J. Fortney⁵ , Vivien Parmentier⁶, Eliza M.-R. Kempton⁷ , Jacob Arcangeli⁸, Jean-Michel Désert⁸ , Brian Kilpatrick⁹ , Laura Kreidberg¹⁰ , and Matej Malik⁷ 

¹ Steward Observatory, University of Arizona, 933 N. Cherry Avenue, Tucson, AZ 85719, USA; meganmansfield@arizona.edu

² School of Earth and Space Exploration, Arizona State University, Tempe, AZ 85281, USA

³ Johns Hopkins University Applied Physics Laboratory, Laurel, MD 20723, USA

⁴ Department of Astronomy & Astrophysics, University of Chicago, Chicago, IL 60637, USA

⁵ Department of Astronomy and Astrophysics, University of California, Santa Cruz, CA 95064, USA

⁶ Department of Physics, University of Oxford, Oxford, OX1 3PU, UK

⁷ Department of Astronomy, University of Maryland, College Park, MD 20742, USA

⁸ Anton Pannekoek Institute for Astronomy, University of Amsterdam, 1098 XH Amsterdam, The Netherlands

⁹ Space Telescope Science Institute, Baltimore, MD 21218, USA

¹⁰ Max Planck Institute for Astronomy, D-69117 Heidelberg, Germany

Received 2021 December 14; revised 2022 March 2; accepted 2022 April 6; published 2022 May 12

Abstract

Secondary eclipse observations of hot Jupiters can reveal both their compositions and thermal structures. Previous observations have shown a diversity of hot Jupiter eclipse spectra, including absorption features, emission features, and featureless blackbody-like spectra. We present a secondary eclipse spectrum of the hot Jupiter WASP-77Ab observed between 1 and 5 μm with the Hubble Space Telescope (HST) and the Spitzer Space Telescope. The HST observations show signs of water absorption indicative of a noninverted thermal structure. We fit the data with both a one-dimensional free retrieval and a grid of one-dimensional self-consistent forward models to confirm this noninverted structure. The free retrieval places a 3σ lower limit on the atmospheric water abundance of $\log(n_{\text{H}_2\text{O}}) > -4.78$ and cannot constrain the CO abundance. The grid fit produces a slightly superstellar metallicity and constrains the carbon-to-oxygen ratio to less than or equal to the solar value. We also compare our data to recent high-resolution observations of WASP-77Ab taken with the IGRINS/IGRINS spectrograph. We find that the best-fit model to the IGRINS data gives a reduced chi squared of $\chi^2_{\nu} = 1.32$ when compared to the WFC3 data. However, the metallicity derived from the IGRINS data is significantly lower than that derived from our self-consistent model fit. We find that this difference may be due to disequilibrium chemistry, and the varying results between the models applied here demonstrate the model dependence of derived metallicities when comparing to low-resolution, low-wavelength coverage data alone. Future work to combine observations from IGRINS, HST, and the James Webb Space Telescope will improve our estimate of the atmospheric composition of WASP-77Ab.

Unified Astronomy Thesaurus concepts: [Hot Jupiters \(753\)](#); [Extrasolar gaseous giant planets \(509\)](#); [Exoplanet atmospheric composition \(2021\)](#)

1. Introduction

Thermal emission measurements taken during secondary eclipse have the potential to reveal information on both the compositions and thermal structures of hot Jupiter atmospheres. The compositions of hot Jupiter atmospheres can be used to track their formation and migration conditions (Venturini et al. 2016; Madhusudhan et al. 2017). For example, a key prediction of the core accretion theory of planet formation is that atmospheric metallicities should be inversely proportional to planet mass (Fortney et al. 2013). Furthermore, the carbon-to-oxygen ratio (C/O) provides information on the mechanisms through which hot Jupiters form and migrate to their current locations (Öberg et al. 2011; Madhusudhan et al. 2014; Mordasini et al. 2016; Ali-Dib 2017; Espinoza et al. 2017; Schneider & Bitsch 2021).

In addition to constraining the composition, secondary eclipse observations can provide information on the thermal structures of hot Jupiters. Theory predicts a continuum of thermal structures and resulting secondary eclipse spectra, which can be divided into three primary categories (Fortney et al. 2008; Parmentier et al. 2018). The coolest hot Jupiters with dayside temperatures (T_{day}) below ≈ 2100 K are predicted to have noninverted temperature-pressure (T - P) profiles, which cause absorption features in their emergent spectra. Hot Jupiters with intermediate temperatures between $2100 < T_{\text{day}} < 2400$ K should have emission features resulting from inverted T - P profiles. Such thermal inversions are predicted to be driven by the presence of a variety of chemical species, such as TiO, VO, FeH, and metal atoms (Hubeny et al. 2003; Lothringer et al. 2018). Finally, the ultrahot Jupiters with $T_{\text{day}} > 2400$ K are expected to also have strongly inverted T - P profiles, but display featureless secondary eclipse spectra in the Hubble Space Telescope (HST)/WFC3 bandpass (1.1–1.7 μm) due to molecular dissociation and H^- opacity (Kitzmann et al. 2018; Lothringer et al. 2018; Parmentier et al. 2018).

These predictions have been borne out through HST observations of absorption features in low-temperature hot

¹¹ NHFP Sagan Fellow.



Jupiters (e.g., WASP-43b, Kreidberg et al. 2014a; and HD 209458b, Line et al. 2016), subtle emission features in medium-temperature hot Jupiters—e.g., WASP-121b (Evans et al. 2017; Mikal-Evans et al. 2020 Mansfield et al. 2021) and WASP-76b (Edwards et al. 2020; Fu et al. 2021; Mansfield et al. 2021)—and blackbody-like spectra in the highest-temperature ultrahot Jupiters—e.g., WASP-18b (Arcangeli et al. 2018; and WASP-103b, Kreidberg et al. 2018). However, not all observed hot Jupiters fit neatly into these three categories. For example, ultrahot Jupiter Kepler-13Ab shows absorption features indicative of a noninverted atmosphere, despite having a high dayside temperature of ≈ 3000 K (Beatty et al. 2017). In general, the population of observed planets shows a scatter in the water feature strengths at a given temperature, which may be caused by variations in atmospheric composition (Mansfield et al. 2021).

In this paper we present the secondary eclipse spectrum of WASP-77Ab observed with HST/WFC3 between 1.1–1.7 μm and Spitzer/IRAC at 3.6 and 4.5 μm . WASP-77Ab is a midtemperature hot Jupiter with an equilibrium temperature of $T_{\text{eq}} = 1705$ K (Maxted et al. 2013), which is near the point where models predict a transition from noninverted T - P profiles creating absorption features to inverted T - P profiles creating emission features (Mansfield et al. 2021). The exact temperature of this transition, however, depends in detail on parameters such as the planet’s atmospheric composition and the amount of heat deposited in its interior. Our observations of WASP-77Ab have double the signal-to-noise of any previous observations at temperatures near this transition, giving us an opportunity to constrain the nature of this transition. We describe our observations and data reduction in Section 2. In Section 3, we perform a 1D free retrieval on our data and compare our data to a set of 1D radiative-convective-thermochemical equilibrium models. Finally, in Section 4 we compare our data to a recent Gemini-S/IGRINS high-resolution thermal emission spectrum of WASP-77Ab, compare the water feature strength of WASP-77Ab to the broader population, and discuss the results of our model fits.

2. Observations and Data Reduction

All of the data presented in this paper were obtained from the Mikulski Archive for Space Telescopes (MAST) at the Space Telescope Science Institute.¹²

2.1. HST/WFC3 Data

We observed two secondary eclipses of WASP-77Ab on 2020 November 7 and 2020 December 19 using the HST/WFC3+G141 grism between 1.1 and 1.7 μm as part of program GO-16168. Each visit consisted of five consecutive orbits in which WASP-77Ab was visible for approximately 52 minutes per orbit. At the beginning of each orbit, we took a direct image of the target with the F126N filter for wavelength calibration.

The observations were taken in the spatial scan mode with the 256×256 subarray using the SPARS25, NSAMP=5 readout pattern, resulting in an exposure time of 89.662 s. We used a scan rate of $0''.195 \text{ s}^{-1}$, which produced spectra extending approximately 153 pixels in the spatial direction

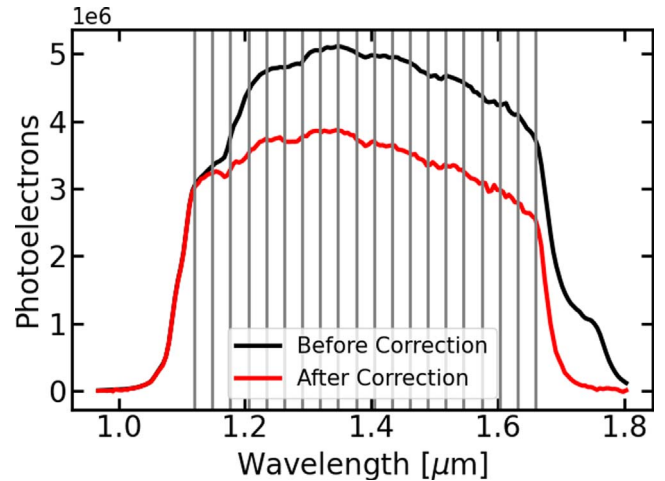


Figure 1. Example stellar spectrum extracted from one spatially scanned exposure taken by HST/WFC3. Black and red lines indicate the extracted flux before and after correcting for the flux of the companion star, WASP-77B, respectively. The spectrum of WASP-77B appears redder in wavelength than that of WASP-77A because its spectral trace was slightly offset in the spectral direction on the detector. Vertical gray lines indicate the extent of the bins for the spectroscopic light curve.

and peak pixel counts of $\approx 37,000$ electrons per pixel. We used bidirectional scans and observed 18 exposures per orbit.

We reduced the data using the data reduction pipeline described in Kreidberg et al. (2014b). We used an optimal extraction procedure (Horne 1986) and masked cosmic rays. To subtract the background out of each frame, we visually inspected the images to find a clear background spot on the detector and subtracted the median of this background area. The uncertainties on the measurements were determined by adding in quadrature the photon noise, read noise, and median absolute deviation of the background.

Following standard procedure for HST/WFC3 eclipse observations, we discarded the first orbit of each visit. The spectra were binned into 19 channels at a resolution $R \approx 40$ –60. Figure 1 shows an example extracted stellar spectrum with the wavelength bins indicated. We also created a broadband white light curve by summing the spectra over the entire wavelength range.

We fit both the white light curve and spectroscopic light curves with the model described in Kreidberg et al. (2014b), which includes an eclipse model (Kreidberg 2015) and a systematics model based on Berta et al. (2012). For the white light curves, the free parameters in the eclipse model were the mideclipse time T_0 and the planet-to-star flux ratio F_p/F_s . For the spectroscopic light curves, the mideclipse time was fixed to the best-fit value from the white light curve ($T_{\text{sec}} = 2455871.12983^{+0.00051}_{-0.00050}$ BJD_{TDB}) and the only free parameter in the eclipse model was F_p/F_s . In both cases, the period, eccentricity, ratio of the semimajor axis to the stellar radius, inclination, and planet-to-star radius ratio were fixed to $P = 1.360030$, $e = 0$, $\frac{a}{R_*} = 5.43$, $i = 89.40$, and $\frac{R_p}{R_*} = 0.13012$, respectively (Turner et al. 2016; Stassun et al. 2017). The instrument systematics model included an orbit-long ramp, whose amplitude and offset were fixed to the same value for both visits, and a normalization constant, visit-long slope, and correction for an offset between scan directions, which all varied between visits. The white light-curve fit thus contained a total of

¹² The specific observations analyzed can be accessed via <https://doi.org/10.17909/gibj-r870>.

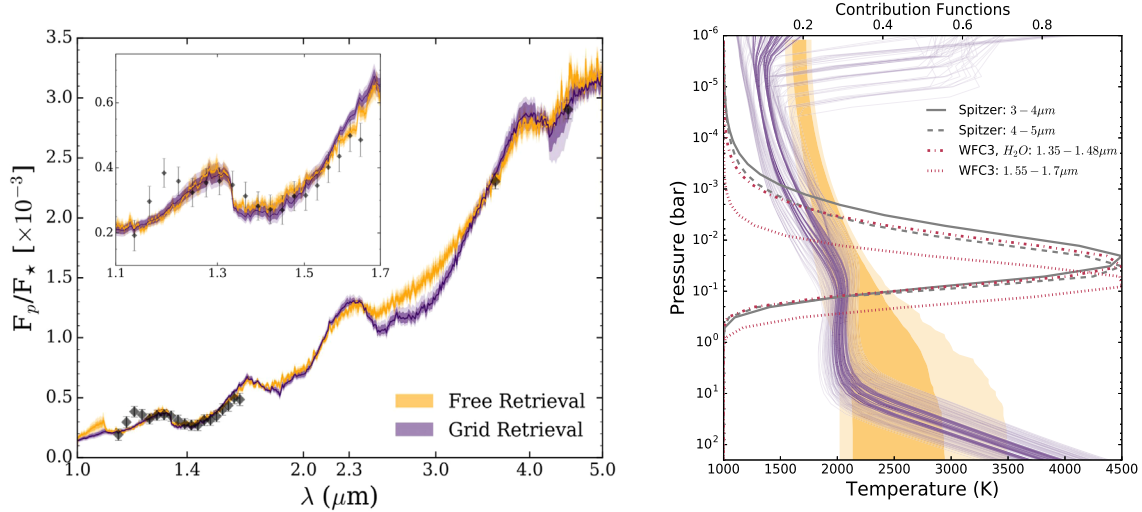


Figure 2. Left: emission spectrum fits using the 1D free retrieval described in Section 3.1, and the Sc-CHIMERA 1D model grid described in Section 3.2. Dark lines represent the median fit, and dark and light shading show 1 and 2σ regions, respectively. Black points show the observations. The inset shows a zoomed in view of the WFC3 segment of the spectrum. The models generally fit the data well, with the best-fit models having reduced chi squared of $\chi^2_{\nu} = 1.12$ for the free retrieval and 1.24 for the grid fit. Right: corresponding pressure-temperature profiles. Grid profiles within 1 and 2σ are shown by dark and light purple lines, respectively. 1 and 2σ regions for the free retrieval are shaded in dark and light yellow, respectively. Contribution functions are also plotted for each Spitzer point, and for in (1.35–1.48 μm) and out (1.55–1.7 μm) of the water feature in the WFC3 wavelength range.

10 free parameters, while the spectroscopic light-curve fits had nine free parameters.

WASP-77A has a companion star, WASP-77B, which has a projected distance large enough that their spectra do not overlap in stare mode. However, the spectra of these two stars overlap during spatial scans. In order to correct for this overlap, we observed a single 0.556 s stare mode exposure with the G141 grism at the beginning of each of the two visits. For each visit, we used the same optimal extraction procedure (Horne 1986) to extract the stare mode spectra of WASP-77A and WASP-77B. We then corrected the observed flux for the presence of the companion star using the equation

$$F_{*,\text{corr}} = F_{*,\text{obs}} \left(\frac{F_A}{F_A + F_B} \right), \quad (1)$$

where $F_{*,\text{corr}}$ is the corrected flux in units of electrons, $F_{*,\text{obs}}$ is the observed flux in units of electrons, and F_A and F_B are the observed fluxes of the primary and companion star in that bandpass, respectively.

We estimated the parameters with a Markov chain Monte Carlofit using the `emcee` package (Foreman-Mackey et al. 2013). The best-fit white light curve had $\chi^2_{\nu} = 4.92$ and an average residual of 90 ppm, which is typical for WFC3 observations of transiting planets orbiting bright host stars. The spectroscopic light curves achieved photon-limited precision, with χ^2_{ν} values between 0.68 and 1.30. The final secondary eclipse spectrum is shown in Figure 2, and Table 1 lists the planet-to-star flux ratio in each channel.

2.2. Spitzer/IRAC Data

The Spitzer Space Telescope observed the WASP-77 system at 3.6 and 4.5 μm under program 13038 (PI: Stevenson). Each phase-curve observation lasted 39.5 hr (starting shortly before secondary eclipse and ending shortly after the subsequent eclipse) and was subdivided into three Astronomical Observation Requests (AORs). The first AOR consisted of a 24 minutes settling period,

Table 1
Secondary Eclipse Spectrum of WASP-77Ab

Wavelength (μm)	F_p/F_* (ppm)
1.120–1.148	192 \pm 47
1.148–1.177	297 \pm 46
1.177–1.205	384 \pm 45
1.205–1.234	359 \pm 44
1.234–1.262	324 \pm 43
1.262–1.291	354 \pm 43
1.291–1.319	359 \pm 42
1.319–1.347	348 \pm 42
1.347–1.376	313 \pm 43
1.376–1.404	283 \pm 43
1.404–1.433	273 \pm 44
1.433–1.461	271 \pm 44
1.461–1.489	313 \pm 45
1.489–1.518	315 \pm 46
1.518–1.546	346 \pm 45
1.546–1.575	402 \pm 47
1.575–1.603	436 \pm 48
1.603–1.632	499 \pm 49
1.632–1.660	486 \pm 51
3.6	2303 \pm 62
4.5	2904 \pm 78

followed by a two science AORs lasting 23 and 16 hr each. The break between science AORs occurred shortly after transit.

We used the Photometry for Orbits, Eclipses, and Transits-data reduction and analysis pipeline (Stevenson et al. 2012; Cubillos et al. 2013; Bell et al. 2021) to derive the secondary eclipse depths reported in this work. For these data, we utilized a 3×3 pixel centroiding aperture to minimize contamination from WASP-77A’s nearby binary companion (WASP-77B) located roughly 2.5 Spitzer pixels away. The standard 5×5 pixel centroiding aperture demonstrated a noticeable bias toward WASP-77B and significant volatility in the measured values. At 3.6 μm , the pointing was stable over the course of

the phase-curve observation. At $4.5 \mu\text{m}$, we measured a drift of 0.5 pixels over the first six hours of observing before stabilizing. The $4.5 \mu\text{m}$ centroids do not overlap with the “sweet spot” mapped out by May & Stevenson (2020) and, thus, we could not use their fixed intrapixel sensitivity map to remove position-dependent systematics.

We tested a range of photometry aperture sizes from 2.0 to 4.75 pixels in 0.25 pixel increments. For each aperture size, we fit the transit, two eclipses, and sinusoidal variation from the planet. Both Spitzer channels use BLISS mapping (Stevenson et al. 2012) to fit the intrapixel sensitivity variations. The $3.6 \mu\text{m}$ observation also requires a rising exponential plus linear ramp to fit the time-dependent systematics and a linear function to fit variations in PRF width along the y direction (PRF detrending; Lanotte et al. 2014). The $4.5 \mu\text{m}$ channel does not exhibit a time-dependent systematic.

The measured eclipse depths decrease systematically with increasing photometry aperture size due to increasing contamination from WASP-77B within the aperture. We use the mean image of each Spitzer observation to estimate the companion flux fraction within each photometric aperture. This process involves masking the flux from WASP-77A, computing the centroid of WASP-77B, and performing aperture photometry on a Spitzer PRF situated at WASP-77B’s centroid position. We then follow the methods describe by Stevenson et al. (2014) to compute corrected eclipse depths. Using CatWISE (Marocco et al. 2021), we estimate the dilution factor to be 0.410 ± 0.013 and 0.405 ± 0.012 at 3.6 and $4.5 \mu\text{m}$, respectively. This calculation is possible since WISE1 and WISE2 have similar bandpasses to IRAC1 and IRAC2. As validation to our methods, we find that the corrected eclipse depths are independent of our choice of aperture size (i.e., they are all consistent within 1σ). Using the apertures that yield the smallest standard deviation of the normalized residuals (3.5 pixels at $3.6 \mu\text{m}$ and 4.5 pixels at $4.5 \mu\text{m}$), we report our final eclipse depths in Table 1.

3. Analysis

We explore fitting the data with a variety of models to test how a gradient of model assumptions impact the derived atmospheric parameters. Here we explore the results from two common modeling philosophies. The first, described in Section 3.1, is the “free” retrieval methodology whereby we fit for the constant-with-altitude abundances for water and carbon monoxide, (the dominant species over the observed wavelengths) and a vertical temperature profile. Within the free retrieval there are no physical/chemical constraints that relate the gas abundances to each other or the temperature profile. The second, described in Section 3.2, is the self-consistent 1D radiative-convective grid model fitting method. This method assumes thermochemical equilibrium chemical abundances for all gases along the temperature-pressure profile, which in turn is dependent upon the opacities and gas abundances. In this framework, rather than retrieving the gas abundances and T - P profile independently, we instead retrieve intrinsic elemental abundances (parameterized with a metallicity and carbon-to-oxygen ratio) and a heat redistribution (which sets the effective stellar flux on the planetary dayside). We explore both of these models throughout this paper because their differing levels of complexity allow us to better understand the nature of the planet’s atmosphere than applying a single model framework alone.

Table 2

Free Parameters and their Prior Ranges (All Uniform) for the Free Retrieval

Parameter	Prior
$\log(n_{\text{H}_2\text{O}})$	$\mathcal{U}(-12, 0)$
$\log(n_{\text{CO}})$	$\mathcal{U}(-12, 0)$
T_0 (K)	$\mathcal{U}(400, 3000)$
$\log P_1$ [log bar]	$\mathcal{U}(-5.5, 2.5)$
$\log P_2$ [log bar]	$\mathcal{U}(-5.5, 2.5)$
$\log P_3$ [log bar]	$\mathcal{U}(-2, 2.5)$
α_1	$\mathcal{U}(0.02, 1.98)$
α_2	$\mathcal{U}(0.02, 1.98)$
$\log(a)$	$\mathcal{U}(-2, 4)$

3.1. 1D Free Retrieval

We performed a nine-parameter free atmospheric retrieval, fitting directly for the volume mixing ratios (constant with pressure) of H_2O and CO , 6 parameters describing the shape of an analytic temperature-pressure profile, and a scale factor (see Table 2 for each model parameter and its prior range, which is uniform for all parameters). The scale factor (a) accounts for any geometric dilution of a dayside hotspot by multiplying the planet-to-star flux ratio by a constant (e.g., Taylor et al. 2021). A value of a close to 1 indicates a more homogeneous dayside, while a smaller value of a indicates a more concentrated hotspot. The temperature-pressure profile is that given by Madhusudhan & Seager (2009), which is a piecewise function of the form

$$T(P) = T_0 + \left(\frac{\log(P/P_0)}{\alpha_1} \right)^{1/\beta_1}, \quad P_0 < P < P_1 \quad (2)$$

$$T(P) = T_2 + \left(\frac{\log(P/P_2)}{\alpha_2} \right)^{1/\beta_2}, \quad P_2 < P < P_3 \quad (3)$$

$$T(P) = T_3, \quad P > P_3 \quad (4)$$

for three atmospheric layers. Layer 1, the upper atmosphere, is between pressures P_0 (the top of atmosphere) and P_1 , and the T - P profile has a slope determined by α_1 and β_1 . Layer 2, the middle atmosphere, is between pressures P_1 and P_3 and has a slope determined by α_2 and β_2 . At pressures greater than P_3 , the profile is isothermal. A third pressure point, P_2 , can be either above or below P_1 , and if $P_2 > P_1$, an inversion will occur. T_2 and T_3 are the temperatures at P_2 and P_3 (determined via continuity), respectively, and T_0 is the top-of-atmosphere temperature. We set $\beta_1 = \beta_2 = 0.5$ to match empirical results, and are left with six free parameters: T_0 , P_1 , P_2 , P_3 , α_1 , and α_2 . While an inversion is not expected for WASP-77Ab, we allow P_2 to range both higher and lower than P_1 .

For the planet’s thermal emission spectrum, we use a pseudo-line-by-line radiative transfer code with absorption cross sections sampled at a resolution $R = \lambda/\Delta\lambda$ of 20,000 (for an introduction to the forward modeling and retrieval frameworks; see Line et al. 2013, 2021). We only include opacities of H_2 - H_2/He CIA, H_2O , and CO . The stellar spectrum is interpolated from the PHOENIX library of model stellar spectra (Husser et al. 2013) and smoothed with a Gaussian filter. Each model spectrum is then binned onto the WFC3 wavelength grid and integrated through the IRAC throughput curves. We used the Python wrapper PyMultiNest (Buchner 2016) for the

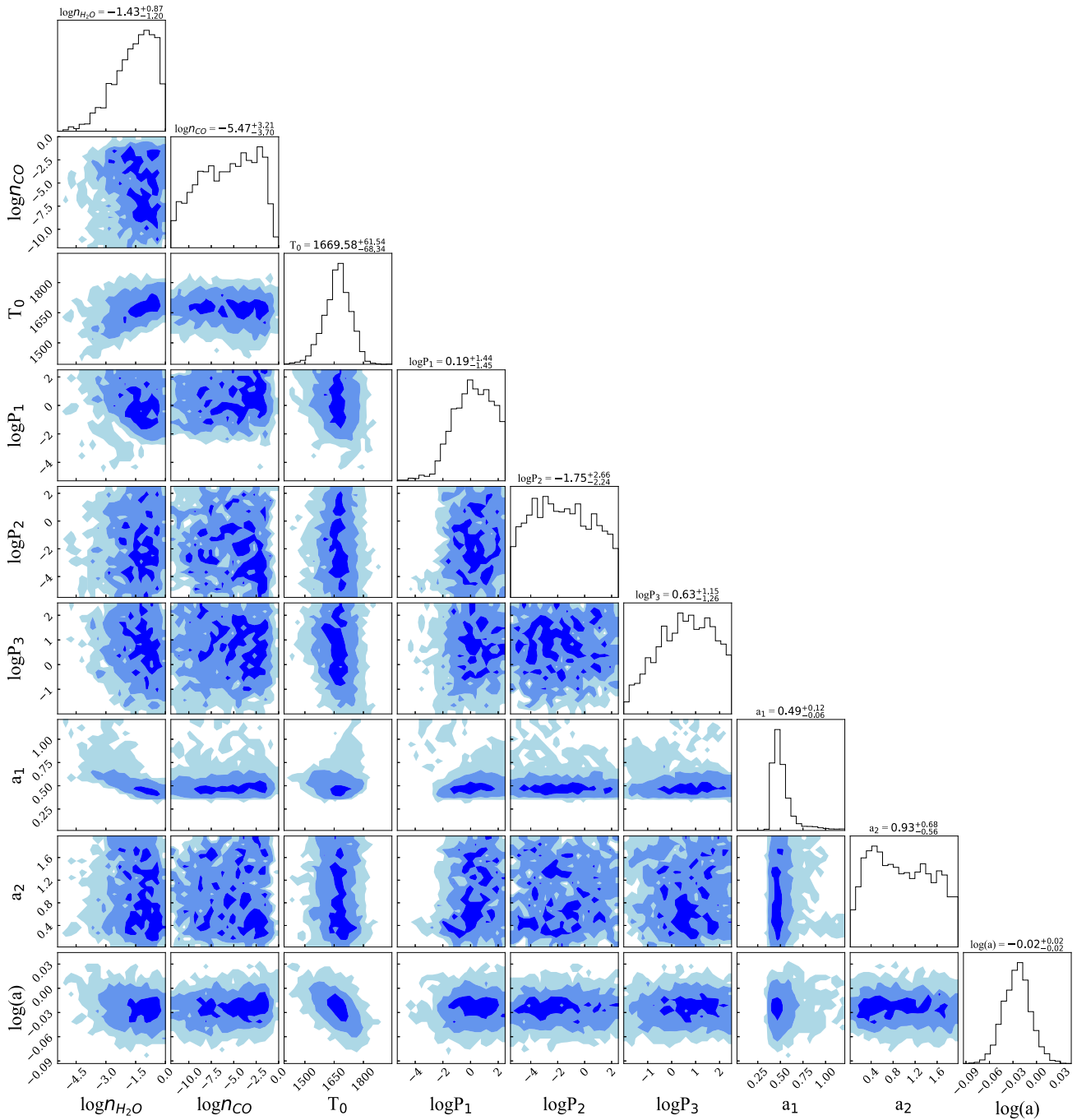


Figure 3. Posterior distributions of all parameters in the free retrieval (Section 3.1). Off-diagonal plots show 2D posterior probabilities for pairs of parameters, with 1, 2, and 3 σ intervals indicated in dark, medium, and light blue. Panels on the diagonal show 1D posterior probability distributions for each parameter. The free parameters include volume mixing ratios of H₂O and CO, 6 parameters for the analytic T - P profile, and a scale factor.

nested sampling algorithm MULTINEST (Feroz et al. 2009) for Bayesian parameter estimation.

Figure 2 shows the measured spectrum for WASP-77Ab with model spectra and T - P profiles randomly drawn from the posterior distribution. Figure 3 contains a corner plot showing the marginal posterior probability distribution of each parameter. The best-fit spectrum has a reduced chi-square metric $\chi^2_{\nu} = 1.12$. We are unable to constrain the abundance of H₂O but can place a robust lower limit at $\log(n_{\text{H}_2\text{O}}) > -4.78$ at 3 σ , whereas CO (and therefore C/O) is entirely unconstrained due to the lack of significant CO spectral features captured by WFC3. Consequently, we can only place a lower limit on the

metal content of the atmosphere at $[(\text{C}+\text{O})/\text{H}] > -1.69$ at 3 σ . The retrieved temperature-pressure profile (Figure 2, right) is monotonically increasing with pressure and has a top-of-atmosphere temperature of 1670^{+62}_{-68} K. The scale factor is 0.95 ± 0.04 , indicative of a homogenous dayside with little to no clouds.

3.2. Comparison to 1D Model Grid

In addition to performing a classic free retrieval, we used Sc-CHIMERA to perform a 1D radiative-convective-thermochemical equilibrium (1D-RC) grid model retrieval, following

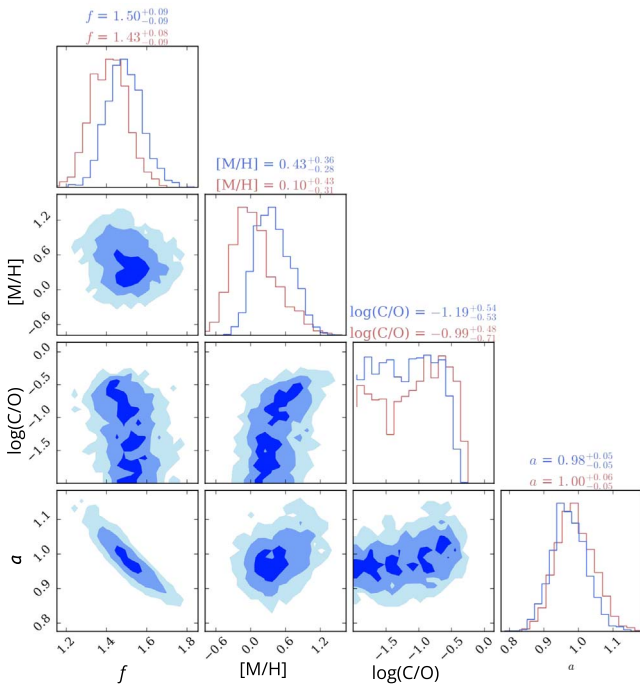


Figure 4. Posterior distributions of free parameters in the 1D Sc-CHIMERA model grid fit for the fit to the full data set (blue) and the fit to the data with the bluest 4 points removed (red). For the full data set, 2D histograms for pairs of parameters are shown in off-diagonal plots with 1, 2, and 3 σ regions shaded in light, medium, and dark blue, respectively. Histograms on the diagonal show 1D posterior probability distributions for each individual parameter.

a similar methodology described in Arcangeli et al. (2018) and Mansfield et al. (2018). We generated a WASP-77Ab specific model grid with free parameters for the global heat redistribution (f), metallicity ($[M/H]$), and C/O. We used the same 1D-RC framework described in Mansfield et al. (2021), which is an upgrade to that used in Arcangeli et al. (2018) and Mansfield et al. (2018). We also include the scale factor (a), which can be included without an additional grid dimension. The grid is coupled to the `pymultinest` nested sampler to perform parameter estimation across f , $[M/H]$, C/O, and a .

We defined prior ranges of 0.4–2.8 for f , -2.0 – 2.6 for $[M/H]$, and 0.01–1.4 for C/O. The heat redistribution factor is defined as in Parmentier et al. (2021) as a function of dayside and equilibrium temperature, $f = (T_d/T_*)^4$. As such, $f=1$ corresponds to full redistribution, $f=2$ corresponds to dayside-only redistribution, and $f=2.67$ is the maximum value allowed by energy conservation. The prior range for f extends beyond possible values to allow `pymultinest` to converge close to maximum and minimum, if needed. The prior range for $[M/H]$ encompasses the range of solar system and exoplanet observations and predictions presented in prior literature (Kreidberg et al. 2014a; Mordasini et al. 2016; Thorngren et al. 2016; Welbanks et al. 2019). The C/O prior range is also defined based on prior literature expectations of $C/O < 1$ (Mordasini et al. 2016).

Figure 2 shows the resulting spectrum and T - P profile for the grid fit, and Figure 4 shows a corner plot for the full posterior. The best grid fit had a reduced chi squared value of $\chi^2_\nu = 1.24$ and showed a noninverted T - P profile. The value of $f = 1.50 \pm 0.09$ retrieved from the fit is consistent with 3D models of cloud-free hot Jupiters at the temperature of WASP-77Ab (Parmentier et al. 2021). The retrieved value of the scale

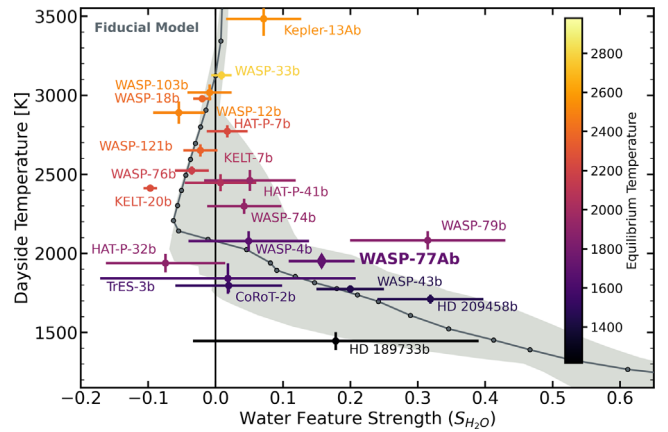


Figure 5. HST water feature strength (S_{H_2O}) and dayside temperature (T_{day}) of WASP-77Ab (bold, diamond point) in the context of all other planets observed between 1.1 and 1.7 μm with HST/WFC3 (colored, circular points; Mansfield et al. 2021; Fu et al. 2022). Both values are calculated following the descriptions in Mansfield et al. (2021). Positive/negative values of S_{H_2O} indicate features observed in absorption/emission, respectively, and a value of $S_{H_2O} = 0$ indicates a featureless, blackbody-like spectrum. The gray points and shaded region show predictions from the 1D model grid presented in Mansfield et al. (2021). WASP-77Ab has $S_{H_2O} = 0.157 \pm 0.049$, indicating the presence of a strong water absorption feature in its spectrum. This value agrees with previously observed trends that planets below $T_{day} \approx 2100$ K tend to have absorption features due to noninverted T - P profiles, but that the scatter in water feature strengths for planets at similar temperatures suggests compositional differences in their atmospheres (Fortney et al. 2008; Parmentier et al. 2018; Mansfield et al. 2021).

factor a was close to 1, which is consistent with the constraint on f because with more heat redistribution we’d expect a less pronounced hotspot. The best-fit metallicity was $[M/H] = 0.43^{+0.36}_{-0.28}$. We note that this metallicity is significantly higher and less precise than the value derived from recent high-resolution observations—see Section 4.2 for a full discussion of these differences. The carbon-to-oxygen ratio is not well constrained, as we do not observe any resolved features of carbon-bearing molecules. However, the fit provides a 2σ upper limit of $C/O = 0.78$, indicating that the planet likely has a solar or subsolar C/O. While the two retrieval methods presented here differ in their estimates of the atmospheric metallicity, they both retrieve a monotonically decreasing T- P profile. We therefore conclude that the noninverted nature of the T- P profile is the most confident result from our analysis. We discuss the differences in retrieved metallicities further in Section 4.2.

4. Discussion

4.1. HST Water Feature Strength

In order to place our observations of WASP-77Ab in the broader context of previous hot Jupiter secondary eclipse observations, we compared the observed water feature strength and derived metallicity to HST/WFC3 observations of other hot Jupiters. We computed the HST water feature strength S_{H_2O} for WASP-77Ab following Equation (1) in Mansfield et al. (2021). The water feature strength for WASP-77Ab is shown in Figure 5 compared to the feature strengths for the data and models presented in Mansfield et al. (2021). We find that the water feature strength of WASP-77Ab fits the previously observed trend, and matches the expectations from the self-consistent models of Mansfield et al. (2021). Additionally, the fact that this planet shows a water feature in absorption at a

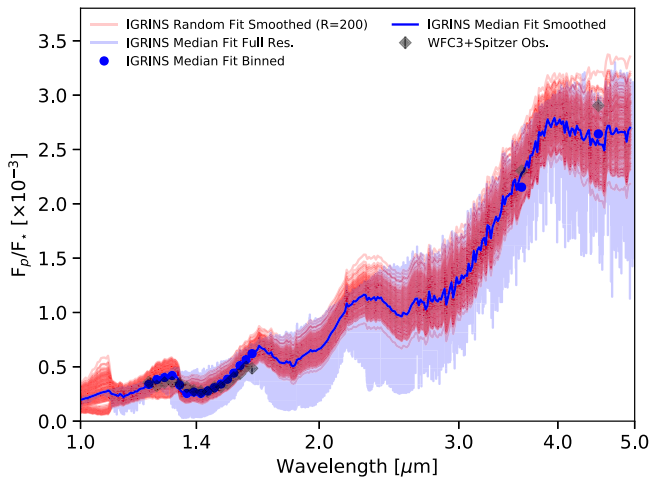


Figure 6. Comparison of our HST/WFC3 and Spitzer emission spectrum of WASP-77Ab (black points) with a fit of dayside emission from high-resolution Gemini-S/IGRINS observation (Line et al. 2021). The blue line and points show the median model fit to the IGRINS data, at full resolution and smoothed to the resolution of the WFC3 data, respectively. Red lines show 500 random draws from the posterior of the high-resolution fit smoothed to an $R = 100$.

dayside temperature of ≈ 1900 K disfavors models with high $C/O \gtrsim 0.7$, low metallicity $[M/H] \lesssim -1.0$, or an amount of internal heating following Thorngren et al. (2019), as such models predict a transition to inverted atmospheres below this temperature.

4.2. Comparison to Gemini-S/IGRINS Results

Confidence in composition and thermal structure inferences is bolstered when independent observations with different instruments arrive at the same conclusions. WASP-77Ab was recently observed near secondary eclipse at high resolution using the IGRINS spectrograph ($R \sim 45,000$) on Gemini-South (Line et al. 2021). These observations spanned a wavelength range of $1.45\text{--}2.55\mu\text{m}$, which allowed them to precisely constrain abundances of both water and carbon monoxide. Figure 6 compares our WFC3 spectrum to the best-fit model from a high-resolution cross-correlation retrieval on these recent IGRINS observations. This plot also shows an ensemble of 500 spectra reconstructed from parameters drawn from the posterior probability distribution of that retrieval.

Figure 6 shows that the WFC3 spectrum falls well within the posterior distribution for the IGRINS model spectra, providing cross-validation for these ground- and space-based observations. Comparing the best-fit IGRINS model to the WFC3 data gives a reduced chi squared of $\chi^2_{\nu} = 1.32$, or a p value of 0.3. This means that if the IGRINS best-fit model were the ground truth we would have a 30% chance of observing the WFC3 data as we did, which demonstrates a remarkable level of consistency between these two data sets. However, the best fit to the high-resolution observations retrieved a metallicity of $[M/H] = -0.48^{+0.15}_{-0.13}$ and a carbon-to-oxygen ratio of $C/O = 0.59 \pm 0.08$ (Line et al. 2021). While their metallicity is consistent with the lower limit from our free retrieval (which is the same retrieval paradigm used in Line et al. 2021), it is inconsistent with the metallicity we derive from the grid fit at 1.8σ .

Figure 7 shows the metallicities of WASP-77Ab derived from the free and grid retrievals compared to the IGRINS result. We investigated what could be driving the discrepancy in derived metallicities between our low-resolution WFC3 and

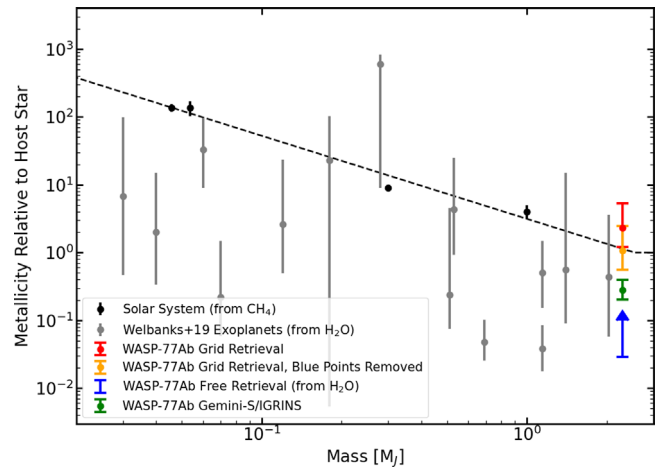


Figure 7. Atmospheric metallicity as a function of planet mass. Black points show solar system planet metallicities, which are based on measurements of $[CH_4/H]$ (Wong et al. 2004; Fletcher et al. 2009; Karkoschka & Tomasko 2011; Sromovsky et al. 2011). The black dashed line shows a fit to the solar system trend, but plateauing at 1 when the planet metallicity equals the stellar metallicity. Gray points show $[H_2O/H]$ for previously observed exoplanets (Welbanks et al. 2019). We additionally compare four measurements of the metallicity of WASP-77Ab: $[M/H]$ from our grid retrieval described in Section 3.2 (red), $[M/H]$ from the grid retrieval on the data with the bluest four points removed (orange, see Section 4.2), $[H_2O/H]$ from our free retrieval described in Section 3.1 (blue, lower limit only), and $[C+O/H]$ from recent high-resolution observations with Gemini-S/IGRINS (green, Line et al. 2021).

Spitzer data and the high-resolution IGRINS data and found that the higher metallicity we derive with our grid fits is driven by the strong downward slope of the bluest points in the WFC3 spectrum. We analyzed the two WFC3 visits independently and found that the downward slope at the blue end of the spectrum is consistent across both visits. We performed a grid fit to the WFC3+Spitzer data with the bluest four points removed and derived a metallicity of $[M/H] = 0.10^{+0.43}_{-0.31}$, which is more consistent with the high-resolution measurement. The results of this fit are shown in Figure 4. This result may indicate that the bluest part of the spectrum, which is not well fit by our equilibrium chemistry models, is influenced by disequilibrium chemistry. However, the lack of precise abundance measurements from our free retrieval demonstrates the difficulty of constraining chemistry in a nonequilibrium model with only low-resolution, low-wavelength coverage data. Alternatively, this discrepancy may just be due to the sensitivity of low-resolution retrieval results to slight changes in the spectral shape. We note that our investigation here is not intended to provide a more accurate or precise metallicity measurement than that derived from the IGRINS observations, but rather to use a comparison of these two data sets to bolster confidence in the high-resolution result and discuss the limitations of deriving abundance constraints from low-resolution data alone. Additionally, techniques for extracting abundance measurements from high-resolution data are relatively new and have only been applied to a couple of data sets, so a comparison to the low-resolution results we present here is useful for assessing the validity of the high-resolution results, even if the low-resolution composition measurements are less well constrained.

We leave a joint retrieval combining our low-resolution HST and Spitzer data and the high-resolution Gemini-S/IGRINS data for a future paper (P. Smith et al. 2022, in preparation). Although it is outside the scope of this paper, such combined












high-resolution and low-resolution fits can constrain the atmospheric composition even more tightly than either data set alone (Brogi & Line 2019). Additionally, in the near future, the James Webb Space Telescope will measure the dayside emission spectrum of WASP-77Ab from 2.87 to 5.10 μm (GTO 1274; PI Lunine). These data will further illuminate the atmospheric composition of WASP-77Ab.

This work was based on observations made with the NASA/ESA Hubble Space Telescope that were obtained from the data archive at the Space Telescope Science Institute (STScI), which is operated by the Association of Universities for Research in Astronomy, Inc. under NASA contract NAS 5-26555. This work also used observations made with the Spitzer Space Telescope, which is operated by the Jet Propulsion Laboratory, California Institute of Technology under a contract with NASA. We acknowledge an anonymous reviewer for helpful comments which improved the manuscript. Support for this work was provided by NASA through the NASA Hubble Fellowship grant HST-HF2-51485.001-A awarded by STScI. M.M. (Mansfield) acknowledges support from a NASA FINESST grant. J.M.D. acknowledges support from the Amsterdam Academic Alliance (AAA) Program, and the European Research Council (ERC) European Unions Horizon 2020 research and innovation program (grant agreement no. 679633; Exo-Atmos). This work is part of the research program VIDI New Frontiers in Exoplanetary Climatology with project number 614.001.601, which is (partly) financed by the Dutch Research Council (NWO).

Facilities: HST (WFC3), Spitzer (IRAC).

Software: batman (Kreidberg 2015), emcee (Foreman-Mackey et al. 2013), matplotlib (Hunter 2007), numpy (van der Walt et al. 2011), pymultinest (Buchner 2016), pysynphot (STScI Development Team 2013), scipy (Virtanen et al. 2021).

ORCID iDs

Megan Mansfield  <https://orcid.org/0000-0003-4241-7413>
 Lindsey Wisner  <https://orcid.org/0000-0002-3295-1279>
 Kevin B. Stevenson  <https://orcid.org/0000-0002-7352-7941>
 Michael R. Line  <https://orcid.org/0000-0002-2338-476X>
 Jacob L. Bean  <https://orcid.org/0000-0003-4733-6532>
 Jonathan J. Fortney  <https://orcid.org/0000-0002-9843-4354>
 Eliza M.-R. Kempton  <https://orcid.org/0000-0002-1337-9051>
 Jean-Michel Désert  <https://orcid.org/0000-0002-0875-8401>
 Brian Kilpatrick  <https://orcid.org/0000-0003-4220-600X>
 Laura Kreidberg  <https://orcid.org/0000-0003-0514-1147>
 Matej Malik  <https://orcid.org/0000-0002-2110-6694>

References

- Ali-Dib, M. 2017, *MNRAS*, 467, 2845
- Arcangeli, J., Désert, J.-M., Line, M. R., et al. 2018, *ApJL*, 855, L30
- Beatty, T. G., Madhusudhan, N., Tsiaras, A., et al. 2017, *AJ*, 154, 158
- Bell, T. J., Dang, L., Cowan, N. B., et al. 2021, *MNRAS*, 504, 3316
- Berta, Z. K., Charbonneau, D., Désert, J.-M., et al. 2012, *ApJ*, 747, 35
- Brogi, M., & Line, M. R. 2019, *AJ*, 157, 114
- Buchner, J. 2016, PyMultiNest: Python interface for MultiNest, Astrophysics Source Code Library, ascl:1606.005
- Cubillos, P., Harrington, J., Madhusudhan, N., et al. 2013, *ApJ*, 768, 42
- Edwards, B., Changeat, Q., Baeyens, R., et al. 2020, *AJ*, 160, 8
- Espinoza, N., Fortney, J. J., Miguel, Y., Thorngren, D., & Murray-Clay, R. 2017, *ApJL*, 838, L9
- Evans, T. M., Sing, D. K., Kataria, T., et al. 2017, *Natur*, 548, 58
- Feroz, F., Hobson, M. P., & Bridges, M. 2009, *MNRAS*, 398, 1601
- Fletcher, L. N., Orton, G. S., Teanby, N. A., Irwin, P. G. J., & Bjoraker, G. L. 2009, *Icar*, 199, 351
- Foreman-Mackey, D., Hogg, D. W., Lang, D., & Goodman, J. 2013, *PASP*, 125, 306
- Fortney, J. J., Lodders, K., Marley, M. S., & Freedman, R. S. 2008, *ApJ*, 678, 1419
- Fortney, J. J., Mordasini, C., Nettelmann, N., et al. 2013, *ApJ*, 775, 80
- Fu, G., Deming, D., Lothringer, J., et al. 2021, *AJ*, 162, 108
- Fu, G., Sing, D. K., Lothringer, J. D., et al. 2022, *ApJL*, 925, L3
- Home, K. 1986, *PASP*, 98, 609
- Hubeny, I., Burrows, A., & Sudarsky, D. 2003, *ApJ*, 594, 1011
- Hunter, J. D. 2007, *CSE*, 9, 90
- Husser, T. O., Wende-von Berg, S., Dreizler, S., et al. 2013, *A&A*, 553, A6
- Karkoschka, E., & Tomasko, M. G. 2011, *Icar*, 211, 780
- Kitzmann, D., Heng, K., Rimmer, P. B., et al. 2018, *ApJ*, 863, 183
- Kreidberg, L. 2015, *PASP*, 127, 1161
- Kreidberg, L., Bean, J. L., Désert, J.-M., et al. 2014a, *ApJL*, 793, L27
- Kreidberg, L., Bean, J. L., Désert, J.-M., et al. 2014b, *Natur*, 505, 69
- Kreidberg, L., Line, M. R., Parmentier, V., et al. 2018, *AJ*, 156, 17
- Lanotte, A. A., Gillon, M., Demory, B. O., et al. 2014, *A&A*, 572, A73
- Line, M. R., Brogi, M., Bean, J. L., et al. 2021, *Natur*, 598, 580
- Line, M. R., Stevenson, K. B., Bean, J., et al. 2016, *AJ*, 152, 203
- Line, M. R., Wolf, A. S., Zhang, X., et al. 2013, *ApJ*, 775, 137
- Lothringer, J. D., Barman, T., & Koskinen, T. 2018, *ApJ*, 866, 27
- Madhusudhan, N., Amin, M. A., & Kennedy, G. M. 2014, *ApJL*, 794, L12
- Madhusudhan, N., Bitsch, B., Johansen, A., & Eriksson, L. 2017, *MNRAS*, 469, 4102
- Madhusudhan, N., & Seager, S. 2009, *ApJ*, 707, 24
- Mansfield, M., Bean, J. L., Line, M. R., et al. 2018, *AJ*, 156, 10
- Mansfield, M., Line, M. R., Bean, J. L., et al. 2021, *NatAs*, 5, 1224
- Marocco, F., Eisenhardt, P. R. M., Fowler, J. W., et al. 2021, *ApJS*, 253, 8
- Maxted, P. F. L., Anderson, D. R., Collier Cameron, A., et al. 2013, *PASP*, 125, 48
- May, E. M., & Stevenson, K. B. 2020, *AJ*, 160, 140
- Mikal-Evans, T., Sing, D. K., Kataria, T., et al. 2020, *MNRAS*, 496, 1638
- Mordasini, C., van Boekel, R., Mollière, P., Henning, T., & Benneke, B. 2016, *ApJ*, 832, 41
- Öberg, K. I., Murray-Clay, R., & Bergin, E. A. 2011, *ApJL*, 743, L16
- Parmentier, V., Line, M. R., Bean, J. L., et al. 2018, *A&A*, 617, A110
- Parmentier, V., Showman, A. P., & Fortney, J. J. 2021, *MNRAS*, 501, 78
- Schneider, A. D., & Bitsch, B. 2021, *A&A*, 654, A71
- Sromovsky, L. A., Fry, P. M., & Kim, J. H. 2011, *Icar*, 215, 292
- Stassun, K. G., Collins, K. A., & Gaudi, B. S. 2017, *AJ*, 153, 136
- Stevenson, K. B., Bean, J. L., Seifahrt, A., et al. 2014, *AJ*, 147, 161
- Stevenson, K. B., Harrington, J., Fortney, J. J., et al. 2012, *ApJ*, 754, 136
- STScI Development Team 2013, pysynphot: Synthetic photometry software package, Astrophysics Source Code Library, ascl:1303.023
- Taylor, J., Parmentier, V., Line, M. R., et al. 2021, *MNRAS*, 506, 1309
- Thorngren, D., Gao, P., & Fortney, J. J. 2019, *ApJL*, 884, L6
- Thorngren, D. P., Fortney, J. J., Murray-Clay, R. A., & Lopez, E. D. 2016, *ApJ*, 831, 64
- Turner, J. D., Pearson, K. A., Biddle, L. I., et al. 2016, *MNRAS*, 459, 789
- van der Walt, S., Colbert, S. C., & Varoquaux, G. 2011, *CSE*, 13, 22
- Venturini, J., Alibert, Y., & Benz, W. 2016, *A&A*, 596, A90
- Virtanen, P., Gommers, R., Oliphant, T. E., et al. 2021, scipy/scipy: SciPy 1.6.3, Zenodo, doi:10.5281/zenodo.4718897
- Welbanks, L., Madhusudhan, N., Allard, N. F., et al. 2019, *ApJL*, 887, L20
- Wong, M. H., Mahaffy, P. R., Atreya, S. K., Niemann, H. B., & Owen, T. C. 2004, *Icar*, 171, 153